

Imaging of magnetic domain walls in iron with a magnetic force microscope: A numerical study

S. Müller-Pfeiffer, M. Schneider, and W. Zinn

Institut für Festkörperforschung, Forschungszentrum Jülich, D-52425 Jülich, Germany

(Received 20 December 1993)

A two-dimensional, numerical, micromagnetic model was applied to understand the images of 180° walls in iron thin films obtained with a magnetic force microscope (MFM). Assuming the tip stray field would not affect the wall magnetization, the model predicts a contrast well below the sensitivity of the MFM. However, this assumption is unrealistic. The inclusion of the tip stray field in the simulation shows that the domain wall is polarized by the tip stray field. The resulting contrasts from the polarized walls differ drastically from the contrasts expected from undisturbed walls but agree well with experimental observations. Such polarization effects make the authors doubtful about the applicability of the MFM to studies of other micromagnetic phenomena in soft magnetic materials.

I. INTRODUCTION

The impressive successes of various scanning probe microscopes such as the scanning tunneling microscope (STM), the atomic force microscope (AFM), and devices derived from them fed hopes of achieving a similar resolution in imaging magnetic structures by means of a scanning probe technique as well. A working magnetic force microscope (MFM) was described by Martin and Wickramasinghe.¹ Subsequent work published by several groups²⁻⁴ was mainly devoted to the imaging of written bit structures in various kinds of magnetic recording materials and to the understanding of the contrast mechanism in magnetic force microscopy.⁵⁻⁷ Attempts to investigate further details of the magnetization structure led to domain wall images in permalloy thin films,⁸ iron whiskers,⁹ and magnetite.¹⁰ After this no more significant results obtained by means of MFM are known to the authors.

Several authors^{9,5} attribute this (lack of) development to circumstances complicating both the acquisition and interpretation of MFM images.

(1) The MFM contrast results from the force (or force gradient) on a tiny ferromagnetic tip in the magnetic stray field emanating from a ferromagnetic sample. To reconstruct the magnetic stray field from the MFM response requires an accurate knowledge of the tip magnetization; in general one does not have this knowledge.

(2) In principle, knowledge of the magnetic stray field is not sufficient for obtaining the magnetization \mathbf{M} of the sample. Under optimal conditions only a map of the magnetic charge density $-\nabla \cdot \mathbf{M}$ can be obtained. A reconstruction of the magnetization \mathbf{M} from this is impossible. To interpret the MFM images, magnetization models for both the sample and the tip have to be assumed, and the calculated MFM response from the models has to be compared with the observed contrast.

(3) The resolution of the MFM is determined by several parameters: the minimal detectable force or force

gradient for a given microscope, the ability to produce "optimal" tips,¹¹ and the ability to operate the MFM at a minimal scanning height. The minimal scanning height mainly depends on the surface roughness, leading to additional contrasts in the image.

(4) The stray field produced by the tip itself can severely disturb the magnetic structure in the sample.

On iron thin films, as an example, we will demonstrate here — in contrast to the claims of other authors^{9,10} — that these peculiarities of the MFM make it impossible to obtain information about the structure of magnetic domain walls in soft magnetic materials using a magnetic force microscope.

II. EXPERIMENTAL DATA

Domain wall observations by means of magnetic force microscopy have been reported by several authors.^{8-10,12} These investigations cover domain walls in Permalloy thin films,⁸ iron whiskers,^{9,12} and magnetite.¹⁰ From their images and from our own experiments with thin epitaxial iron films of several thicknesses—a representative image is shown in Fig. 1—several general observations can be made.

(1) The contrast of a 180° domain wall far from a fork into two 90° walls and far from Bloch lines always appears to be *white* in the image, i.e., the contrast is caused by an *attractive* interaction between the wall and the tip. In all our experiments with films of different thicknesses we never found dark contrasts. With respect to the different symmetry of the walls (Néel walls, Bloch walls) one would expect different kinds of contrasts. For instance, depending on the chirality of the wall one would expect both segments showing white (attractive interaction) and dark contrast (repulsive interaction).

(2) The contrast caused by a magnetic domain wall in a MFM is approximately $1 \mu\text{m}$ wide, quite independent

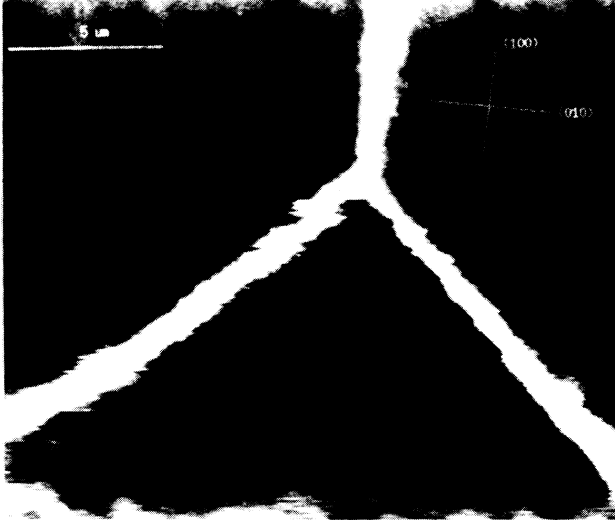


FIG. 1. MFM image of a 180° (Bloch) wall forking into two 90° walls in a 50 nm thick Fe (100) film. The film was covered by 30 nm ZnS. The scanning height was about 50 nm above the outer ZnS surface. According to our experiments, all noncharged walls give the same white contrasts.

of the peculiarities of the experimental setup (i.e., tip shape, scanning height, MFM operation mode, etc.) and the investigated material and wall type.

(3) As demonstrated by Mamin *et al.*,⁸ the tip stray field in their magnetic force microscope is able to distort and move domain walls in a Permalloy thin film.

To evaluate the theoretical force curves correctly, one should keep in mind the instrumental limits of the force microscope in the noncontact operation mode. First, the minimal detectable force is given by the sensitivity of the detector measuring the tip displacement. For commonly used cantilevers (spring constant approximately 1 N/m) and commonly used displacement sensors (resolution approximately 1 Å) the estimated minimal detectable force is around 10^{-10} N. One should note that for softer cantilevers the thermally induced noise is the limiting factor.

In the dynamic operation mode the sensitivity is determined by the minimal detectable shift of the cantilever's resonance frequency. Operating a monocrystalline cantilever in vacuum and using a sophisticated frequency detection scheme, for a cantilever's resonance frequency of 100 kHz a resolution of 0.1 Hz can be achieved.¹³ Following Ref. 13, with this setup an ultimate sensitivity of $F'_{\min} = 2 \times 10^{-6}$ N/m can be reached. In both operation modes a bandwidth of 1000 Hz was assumed. This guarantees image acquisition in a reasonable time, i.e., in some minutes.

III. NUMERICAL MODEL

In order to calculate the magnetic stray fields for various domain wall configurations in single layers, a two-dimensional, numerical micromagnetic model was used. From the equilibrium configuration found by this model

the magnetic stray field—and consequently the MFM contrast—can be calculated.

The employed numerical model follows the ideas developed by Brown and LaBonte,¹⁴ LaBonte,¹⁵ and Aharoni.¹⁶ Additionally, several modifications proposed later by other authors^{17,18} to improve the computational performance have been adopted as well.

The minimum of the total energy is found by time integration of the Landau-Lifshitz-Gilbert equation (LLG) without precession term in dimensionless form

$$\frac{d\mathbf{m}}{dt'} = -\mathbf{m} \times (\mathbf{m} \times \mathbf{h}_{\text{eff}}), \quad (1)$$

with the reduced magnetization $\mathbf{m} = \mathbf{M}/M_s$, the reduced effective field $\mathbf{h}_{\text{eff}} = \mathbf{H}_{\text{eff}}/M_s$, and the reduced time $t' = t M_s^2/\alpha$, where M_s is the saturation magnetization and α the original damping parameter from the LLG. We assumed that the magnetization $M_s = |\mathbf{M}|$ is constant throughout the ferromagnet. Omitting the precession term is justified because we are not interested in the dynamics of the approach to the equilibrium, but only in the equilibrium itself.

The model system is a slab of width a (x direction) and height b (z direction) extending infinitely in both directions along the y axes. This slab is subdivided in $N_x \times N_z$ quadratic prisms. The magnetization \mathbf{m}_{ij} inside the prisms (i, j) is kept constant. Von Neumann type boundary conditions ($\partial\mathbf{m}/\partial\mathbf{n} = 0$) are chosen, i.e., the surface anisotropy has been neglected in the present model.

The effective magnetic field is derived from the total energy density

$$\mathbf{H}_{\text{eff}} = \frac{\partial e_{\text{tot}}}{\partial \mathbf{M}}. \quad (2)$$

The effective field includes exchange, anisotropy, external, and demagnetizing fields. The total energy density used in this study is composed of the following terms.

(1) The exchange energy density

$$e_{\text{exch}} = A (\nabla \mathbf{M})^2, \quad (3)$$

where A is the exchange stiffness, (2) the magnetocrystalline anisotropy energy density

$$e_{\text{anis}} = K_c (M_x^2 M_y^2 + M_y^2 M_z^2 + M_z^2 M_x^2), \quad (4)$$

where we considered a cubic anisotropy as for iron, (3) and the Zeeman energy density

$$e_{\text{ext. field}} = -\mu_0 \mathbf{M}(\mathbf{r}) \cdot \mathbf{H}_{\text{ext}}(\mathbf{r}). \quad (5)$$

One should note that the external field is not necessarily homogeneous. (4) Finally, the energy density of the demagnetizing field is needed,

$$e_{\text{demag}} = -\frac{1}{2} \mu_0 \mathbf{M} \cdot \mathbf{H}_d. \quad (6)$$

The numerical calculation of the demagnetizing field \mathbf{H}_d is the computationally most extensive part of the simulation. Special measures must be applied to speed up this

part of the computation.

Magnetostriction has been omitted in the present model. Despite the presence of cubic anisotropy in the model, this approximation does not lead to a decay of the 180° wall into two 90° walls. In a system with a boundary as described here, such structure would produce a large magnetostatic stray field, which is energetically unfavorable.

Now the effective fields for the finite-mesh system can be derived from the energy terms (3)–(6) using the definition (2) and the approximations of the derivatives on a mesh. The exchange contribution to the effective field for the nonboundary cells becomes

$$\mathbf{h}^{\text{exch}}(i, j) = \frac{2A}{\mu_0 M_s^2 \Delta^2} [\mathbf{m}(i+1, j) + \mathbf{m}(i-1, j) + \mathbf{m}(i, j+1) + \mathbf{m}(i, j-1) - 4\mathbf{m}(i, j)], \quad (7)$$

with Δ denoting the mesh size. For boundary cells, the boundary conditions should be taken into account.

The discretization of the crystal field anisotropy is straightforward:

$$h_x^{\text{anis}} = -\frac{2K_c}{\mu_0 M_s^2} m_x(i, j) [m_y(i, j)^2 + m_z(i, j)^2]. \quad (8)$$

The other components can be obtained from (8) by means of cyclic exchange of the indices.

If $\mathbf{h}_d(i, j; k, l)$ denotes the stray-field contribution generated by $\mathbf{m}(k, l)$ inside the mesh (i, j) , if $(i, j) \neq (k, l)$, and if we assume that all cells have a quadratic cross section and identical size, $\mathbf{h}_d(i, j; k, l)$ can be calculated as follows:

$$h_x^d(i, j; k, l) = A(k-i, l-j) m_x(k, l) + C(k-i, l-j) m_z(k, l), \quad (9)$$

$$h_z^d(i, j; k, l) = C(k-i, l-j) m_x(k, l) - A(k-i, l-j) m_z(k, l). \quad (10)$$

The formulas for $A(i, j)$ and $C(i, j)$ are given in the Appendix. The self-field, i.e., the field inside the mesh generated by the magnetization of the mesh itself, will be included separately. As a consequence, we can assume $A(0, 0) = 0$ and $C(0, 0) = 0$. Summing (9) and (10) and including the self-field we get

$$h_x^d(i, j) = \sum_{k,l} [A(k-i, l-j) m_x(k, l) + C(k-i, l-j) m_z(k, l)] - \frac{1}{2} m_x(i, j), \quad (11)$$

$$h_z^d(i, j) = \sum_{k,l} [C(k-i, l-j) m_x(k, l) - A(k-i, l-j) m_z(k, l)] - \frac{1}{2} m_z(i, j). \quad (12)$$

A straightforward calculation of these formulas is computationally extremely extensive. The computation of

the whole demagnetizing field needs on the order of $(N_x \times N_z)^2$ floating point multiplications. However, the sums in (11) and (12) have the form of a convolution. As well known¹⁹ and already demonstrated in numerical micromagnetics,^{17,18} the computation of convolution sums for large data fields can be substantially speeded up using the convolution theorem and fast Fourier transformation (FFT). This is mainly based on the fact that FFT on a field with N points can be done in $N \log_2 N$ steps. For large N this is much less than N^2 .

Due to the quadratic cross section of the meshes, the calculation of both x and z components of the demagnetizing field can be performed at once using complex numbers,

$$\tilde{m} = m_x + im_y, \quad (13)$$

$$\tilde{h}_d = h_x^d + ih_y^d + \frac{1}{2}\tilde{m}, \quad (14)$$

where $\frac{1}{2}\tilde{m}$ was added to compensate the self-field of each prism. The self-field will be restored after the convolution. Applying the convolution theorem, it follows that

$$\hat{h}_d = [\hat{a}(\mathbf{k}) + \hat{c}(\mathbf{k})] \hat{m}^*(-\mathbf{k}), \quad (15)$$

where $\hat{m}(\mathbf{k})$, $\hat{h}_d(\mathbf{k})$, $\hat{a}(\mathbf{k})$ and $\hat{c}(\mathbf{k})$ are the Fourier transforms of \tilde{m} , \tilde{h}_d , $A(i, j)$, and $C(i, j)$, respectively; the asterisk denotes complex conjugation. From (15), the demagnetizing field can be calculated for the real space by means of inverse FFT and adding the self-field for each prism.

Further, the boundary conditions have to be considered. We use von Neumann boundary conditions ($\partial \mathbf{m} / \partial \mathbf{n} = 0$). The boundary conditions are obeyed as follows: the grid is continued outside the actual boundary by mirroring as seen in Fig. 2. Therefore the exchange field (7) for the boundary cells must be replaced by

$$\mathbf{h}_{\text{boundary}}^{\text{exch}}(i, j) = \frac{2A}{\mu_0 M_s^2 \Delta^2} [\mathbf{m}(i+1, j) + \mathbf{m}(i-1, j) + \mathbf{m}(i, j \pm 1) - 3\mathbf{m}(i, j)]. \quad (16)$$

Here the $+$ sign is valid for the boundary layer at the bottom side of the slab and the $-$ sign is valid for its top side.

Now the right-hand side of Eq. (1) is complete. The numerical integration of (1) is performed using an adap-

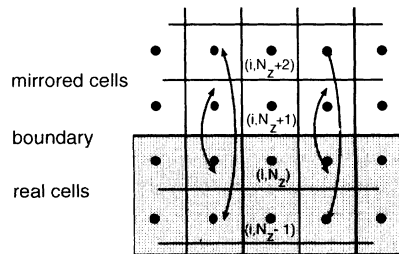


FIG. 2. The boundary condition $\partial \mathbf{m} / \partial \mathbf{n}$ can be fulfilled by a continuation with mirrored cells outside the actual boundary.

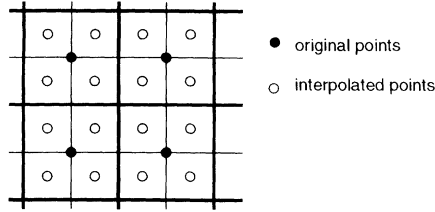


FIG. 3. The starting configuration for the finer grid (thin lines, hollow circles) is generated from the cruder one (thick lines, filled circles) by a bicubic interpolation.

tive step size, fourth-order Runge-Kutta method.¹⁹ The initial state is chosen carefully because the final magnetization state usually has the same symmetry as the initial one. This could result in an unphysical metastable state.

After each integration step, it is verified that the total energy of the system really has decreased. If this is the case, the integration step is accepted, otherwise the step is repeated with reduced step size. This procedure is continued until the condition

$$\max_{ij} |\mathbf{m} \times (\mathbf{m} \times \mathbf{h}_{\text{eff}})| < \epsilon \quad (17)$$

is fulfilled. Typically ϵ is chosen as 10^{-4} .

A further procedure employed in this simulation is the stepwise refinement of the grid: for a given grid the above described procedure is executed until the condition (17) is reached. Then a new grid is generated with four times as many meshes as before ($2N_x \times 2N_z$). The initial state of the new grid is obtained from the old one by bicubic interpolation as shown in Fig. 3. Then, on the refined grid, the described relaxation procedure is continued until condition (17) is reached again. The whole procedure—grid refinement and subsequent relaxation—is repeated until the final grid resolution is reached.

The described procedure has been implemented on a workstation. Even for relatively large systems (256×64 cells), the code ran fast enough to get a result within hours.

IV. RESULTS

Figure 4 shows the structure of an asymmetric Bloch wall in a 500 nm thick iron slab with the wall running along the slab axis. The modeled system was a $2 \mu\text{m}$ wide and 500 nm thick iron slab. The following model parameters have been used: exchange stiffness $A = 2.1 \times 10^{-11}$ J/m, saturation magnetization $M_s = 1.7 \times 10^6$ A/m, and cubic anisotropy constant $K_c = 4.7 \times 10^4$ J m⁻³. The boundary conditions at the right and the left side are chosen for a free boundary ($\partial \mathbf{m} / \partial \mathbf{n} = 0$). This was done to evaluate whether the system is large enough to represent an infinitely wide thin film fairly well. The system is assumed to be large enough if there are no surface charges at the side faces.

The simulation usually started with 32×8 cells and was finished with 128×32 meshes. Both N_x and N_z are pow-

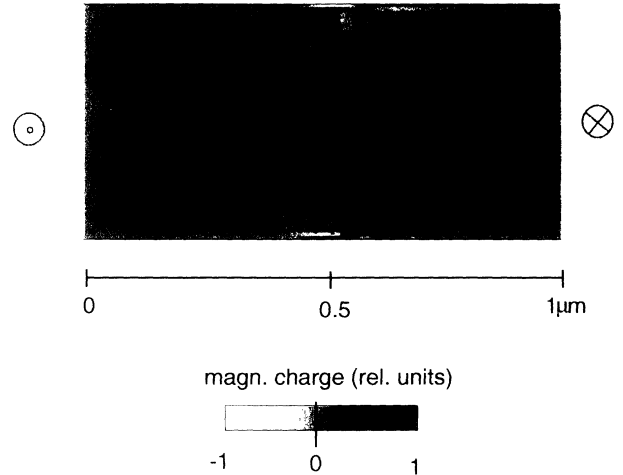


FIG. 4. Asymmetric Bloch wall in a $500 \text{ nm} \times 2000 \text{ nm}$ (100) iron slab as calculated by the model. The final grid had 256×64 cells. The picture shows only the central part ($0.5 \mu\text{m} \times 1 \mu\text{m}$) of the slab. The cells are rendered according to the magnetic charge distribution while the arrows show the projection of the magnetization \mathbf{m} into the x - z plane. In the figure only the central part of the system containing the wall is shown.

ers of 2 with respect to the application of FFT to the computation of the magnetic stray field.

The arrows in the figure show the projection of the magnetization \mathbf{m} into the x - z plane, while the gray scale shows the magnetic charge density $\rho = -\nabla \cdot \mathbf{m}$. A medium gray indicates the absence of charges while dark and light areas indicate positive and negative charge densities respectively.

The uncompensated magnetic charges are responsible for the magnetic stray field. One can see that the magnetic charges appear only in a small area around the flux closure vortices near both surfaces of the thin film. That is, in thick films or bulk crystals, the inner parts of a Bloch wall do not contribute to the magnetic stray field at all.

The flux closure vortex is not symmetric. The analytical model proposed by Hartmann⁹ to understand the domain wall images in a MFM is based on the assumption that the wall is everywhere symmetric. This behavior could not be confirmed by our model, by the model calculations of Scheinfein *et al.*,²⁰ nor by earlier work of Hubert.²¹

Because the scanning area is usually large compared to the characteristic size of the flux closure vortex in an iron system, the charge distribution in the vortices can be decomposed into multipoles and the resulting multipole field from the upper and lower vortex will be used to calculate the MFM contrast. Following this path, the charge distribution inside the vortex is decomposed up to the second order and omitting higher orders as follows:

$$\rho(\mathbf{r} + \mathbf{r}') = \rho(\mathbf{r}) + \mathbf{r}' \cdot \nabla \rho(\mathbf{r}) + \frac{1}{2} \sum_{ij} \frac{\partial^2}{\partial r_i \partial r_j} \rho(\mathbf{r}) r'_i r'_j, \quad (18)$$

where r_i and r'_i are the i th component ($i \in \{x, y, z\}$) of \mathbf{r} and \mathbf{r}' , respectively, and $\mathbf{r}' \ll \mathbf{r}$. If $f(\mathbf{r})$ is Green's function for the potential problem, i.e., $f(\mathbf{r}) = \ln|\mathbf{r}|$ for the two-dimensional problem, the potential of the magnetic field generated by the charge distribution can be written as

$$\Phi(\mathbf{r}) = \frac{M_s}{2\pi} \int f(\mathbf{r} - \mathbf{r}') \rho(\mathbf{r}') d\mathbf{r}', \quad (19)$$

$$\Phi(\mathbf{r}) \approx \frac{M_s}{2\pi} \left[\underbrace{f(\mathbf{r}) \int \rho(\mathbf{r}') d\mathbf{r}'}_{\text{magn. charge}} + \underbrace{\nabla f(\mathbf{r}) \int \mathbf{r}' \rho(\mathbf{r}') d\mathbf{r}'}_{\text{dipolar moment}} + \frac{1}{2} \sum_{ij} \frac{\partial^2}{\partial r_i \partial r_j} f(\mathbf{r}) \underbrace{\int r'_i r'_j \rho(\mathbf{r}') d\mathbf{r}'}_{\text{quadrupolar moment}} \right]. \quad (20)$$

The magnetic charge and dipolar and quadrupolar moments will be determined numerically from the simulated structures. As a consequence, we obtain the stray field from (20) as an analytical expression containing only a few numerical parameters, which is favorable in comparison to a pure numerical result. This potential is used to compute the MFM response in the following.

A. MFM response of an undisturbed wall

With the above outlined method we calculate the MFM contrast for the following model systems: (1) a 125 nm and a 500 nm thick iron film with an asymmetric Bloch wall, (2) a 5 nm thick iron film with a Néel wall, and (3) a semi-infinite (i.e., bulk) iron system such as a whisker, also with a Bloch wall. First, we calculate the expected MFM contrast under the assumption that the stray field of the tip does not influence the magnetization structure of the wall.

Because the typical size of the magnetic tip is small in comparison with the scanning area, the tip will be represented by either a magnetic monopole or a magnetic dipole. The first will be a model for an etched Ni wire magnetized along its axis and the second—to some extent—for a nonmagnetic cantilever covered by a magnetic film. The monopole will carry the same magnetic charge as the end of a Ni prism with a quadratic cross section and 30 nm edge length magnetized along its axis while the dipole will have the same dipolar moment as a cube of 30 nm edge length magnetized in the z direction.

Following this program, calculated MFM wall profiles for some typical cases are displayed in Figs. 5, 6, and 7. It can be seen from the figures that generally the force on a monopole probe as described above, scanning over a Bloch wall in an iron thin film, does not exceed 10^{-11} N. This is one order of magnitude below the ultimate sensitivity of the MFM in the static operation mode. The maximum force on the monopole tip above the simulated Néel wall is 2.3×10^{-11} N, which is below the sensitivity limit as well. Further, it can be stated that the force on the dipolar probe is less above the Bloch wall or approximately equal above the Néel wall compared to the force on a monopolar probe under the same conditions.

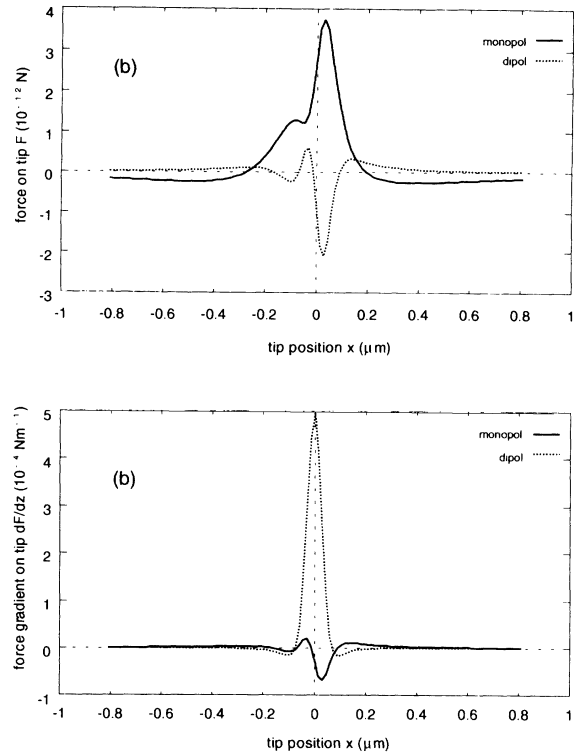


FIG. 5. Calculated wall contrast profiles of the asymmetric Bloch wall in 500 nm iron as shown in Fig. 4. The graphs show force (a) and force gradient (b) for monopolar and dipolar probes.

The behavior of the force gradient is opposite, i.e., the dipolar probe generally yields a somewhat higher (or at least comparable) signal than the monopolar probe. Generally the force gradient is in the order of magnitude 10^{-3} N/m, which is well above the sensitivity limit of the force gradient, calculated under optimistic conditions. However, we will see in the next subsection that the assumption that the tip stray field would not disturb the wall structure does not hold.

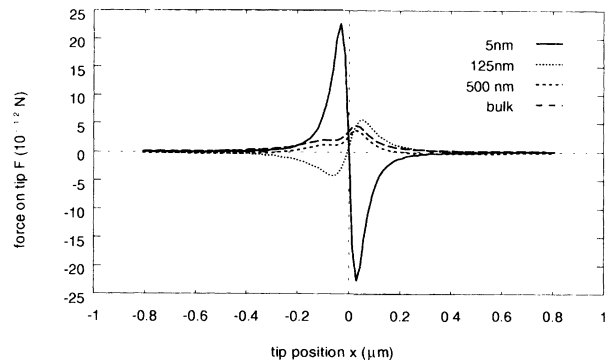


FIG. 6. Calculated force profile obtained with a monopolar probe as described over a Néel wall in 5 nm iron film and asymmetric Bloch walls in 125 nm and 500 nm thick films and in a semi-infinite (i.e., bulk) system. The asymmetric Bloch walls have the flux closure vortices both at one side of the wall center.

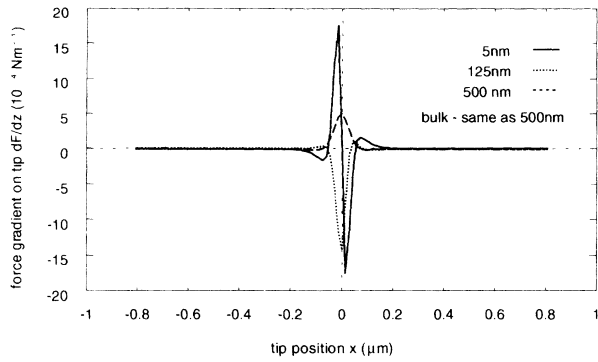


FIG. 7. Calculated force gradient profile obtained with a dipolar probe for the same systems as in Fig. 6.

Furthermore, depending on the actual symmetry of the imaged asymmetric Bloch wall, one would expect different types of wall contrasts as can be seen from Fig. 8. These different types of wall contrasts have not been found in the experiments.

The actual width of the wall contrast can reach $1 \mu\text{m}$, which corresponds to the experimental observations.

B. Polarization of walls by tip stray field

The same procedure as described before can be repeated, considering the tip stray field as an external

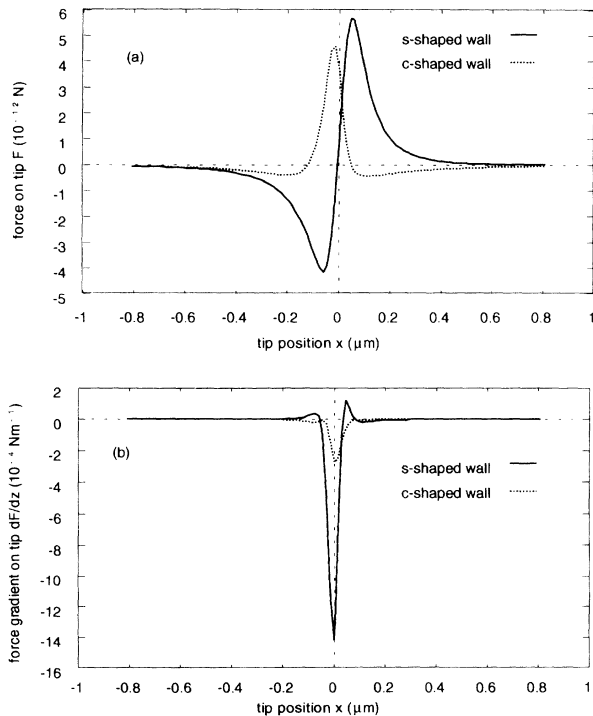


FIG. 8. Calculated contrasts (force mode, monopolar probe) for Bloch walls with different symmetries in 125 nm thick Fe films. “c-shaped” means that the flux closure vortices at the top and at the bottom of the slab are on one side of the wall center, “s-shaped” means that they are at different sides.

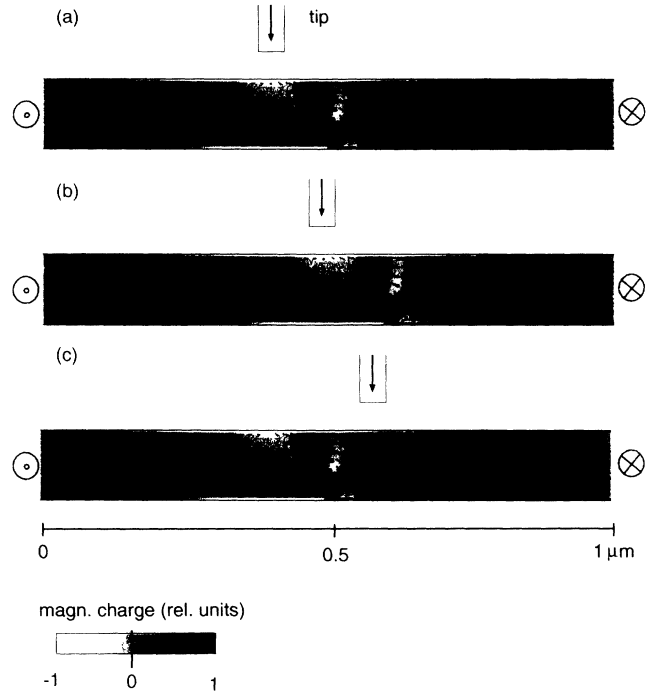


FIG. 9. Series of profiles for polarized walls. The polarization is caused by the tip stray field; the tip position above the sample is varied. The tip is simulated by a 50 nm wide Ni stripe of infinite extent in the z direction and scanning 50 nm above the sample surface. The magnetic charges compensating the charges in the image reside at both side faces and are not shown therefore, because only the central part ($1 \mu\text{m}$) of the $2 \mu\text{m}$ wide slab of the slab is shown.

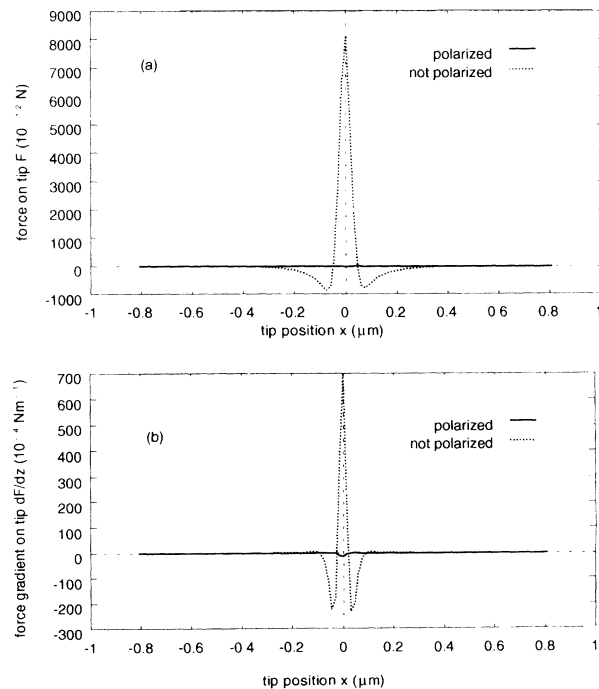


FIG. 10. Comparison of calculated wall contrast profiles between nonpolarized and polarized walls. The polarized wall is the same as in Fig. 9(b) with a tip position above the center of the slab in the x direction.

field. A real micromagnetic model of the tip-wall interaction has to be a three-dimensional one. However, some essential information can be obtained from a two-dimensional model as well. The main shortcoming is that the two-dimensional “tip” is more like a blade. The bladelike shape of the tip is a direct consequence to the two-dimensionality of the model, i.e., the tip must have the same translational symmetry as the wall in the y direction.

In the present simulation, the tip stray field is generated by a semi-infinite (i.e., infinitely extending in the y direction), 50 nm thick Ni stripe, homogeneously magnetized in the z direction. The end of the stripe is located 50 nm above the film surface. Compared to a point source, this setup gives a more realistic magnetic field near the source. One should note that the maximum external field is mainly determined by the saturation magnetization of the tip material. Consequently, changing the tip width would alter the disturbed area rather than the strength of the disturbance.

In Fig. 9 we see a series of magnetization configurations in a 125 nm thick iron slab, where the position of the tip differs. The series was generated in the following way: First, the configuration with the leftmost tip was generated from scratch. Then the left equilibrium configuration was taken as the starting point for its right neighbor. In the figure between subsequent states one intermediate state has been omitted. We believe that this procedure simulates to some extent the scanning of the tip over the domain wall.

Several observations can be made from the figure: The tip stray field disturbs the domain wall configuration drastically, especially if we pay attention to the magnetic charge distribution. We observe a very long range disturbance of the wall structure leading to magnetic charges

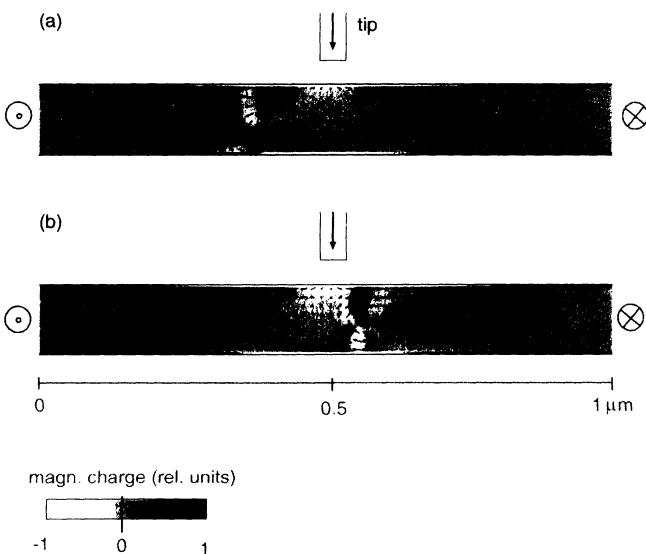


FIG. 11. A polarized counterclockwise rotating wall (b) and a polarized clockwise rotating wall (a) are both polarized by the tip stray field. The wall position differs with respect to the tip position.

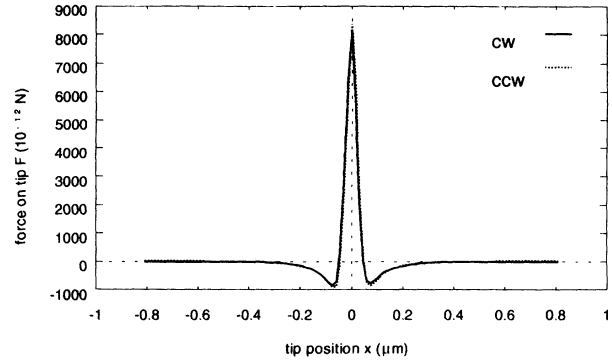


FIG. 12. A polarized counterclockwise rotating wall (ccw) and a polarized clockwise rotating wall (cw) yield almost the same contrast for the MFM.

mostly of one sign under the tip while the charges of the opposite sign are moved to the right and left edges of the sample. Further, the wall is moved by the moving tip.

To estimate the impact of the wall polarization on the MFM response, from one of the disturbed configurations the signal was calculated using the same method as described above. The result is shown in Fig. 10. The signal of the disturbed wall is almost four orders of magnitude larger than the signal generated by a nondisturbed wall. It is therefore possible to observe these stray-field artifacts of walls even in the static operation mode. The wall scan is approximately 1 μm wide, as we observed in the experiment. The wall polarization explains the persistent appearance of white wall contrasts, indicating an attractive interaction. Figure 11 shows the polarization of both a clockwise (a) and a counterclockwise (b) turning wall. In both cases the wall structure is severely disturbed and large uncompensated amounts of magnetic charge can be seen in the wall region. The wall position with respect to the tip is different. As shown in Fig. 12 both configurations lead to almost the same contrasts.

This behavior cannot be explained by the opposite process, the polarization of the tip by the wall’s stray field. The stray field of the polarized wall is smaller than the stray field of the tip. Moreover, the mutual polarization favors a tip magnetization along the tip’s axis. This statement is to be confirmed by a more comprehensive model including the micromagnetics of the tip as well.

V. CONCLUSIONS

A two-dimensional, numerical micromagnetic model was used to investigate the imaging process in the MFM for the model system monocrystalline iron. Under the assumption that the tip stray field does not disturb the wall structure, it could be shown that only in the dynamic operation mode of the MFM under optimal conditions can the walls be imaged. However, if we take into account the interaction between tip and sample, the simulations showed that the wall is polarized by the tip stray field. After that, the walls are visible, but the contrasts do not depend on the undisturbed wall structure. This

effect cannot be avoided. Consequently, the simulations showed that it is not possible to use the magnetic force microscope to study the fine structure of undisturbed domain walls in iron. Moreover, the authors are pessimistic about applicability of the MFM for the investigation of micromagnetic structures in other soft magnetic systems.

ACKNOWLEDGMENTS

This work was financially supported by the SmMmS project of the European Community. The authors are grateful to R. Schreiber (Jülich) for the sample preparation, A. Hubert (Erlangen University) for some helpful discussions, and R. Mueller (Jülich) for critically reading the manuscript.

APPENDIX: INTERACTION COEFFICIENTS

The interaction coefficients $A(i, j)$ and $C(i, j)$ are calculated as follows. First the potential $\phi(i, j) =$

$\Phi(i, j)/M_s$ caused by a mesh at (i, j) is determined,

$$\Phi = m_x \int_{j-\frac{1}{2}}^{j+\frac{1}{2}} [f(i + \frac{1}{2}, j + y) - f(i - \frac{1}{2}, j + y)] dy + m_z \int_{i-\frac{1}{2}}^{i+\frac{1}{2}} [f(i + x, j + \frac{1}{2}) - f(i + x, j - \frac{1}{2})] dx, \quad (\text{A1})$$

where $f(x, y) = -\frac{1}{4\pi} \ln(x^2 + y^2)$. Then $A(i, j)$ and $C(i, j)$ are derived by differentiating (A1) and comparing the result with (11) and (12). Collecting the coefficients with m_x and m_z yields

$$A(i, j) = \arctan \frac{2(2i-1)}{(2i-1)^2 + 4j^2 - 1} - \arctan \frac{2(2i+1)}{(2i+1)^2 + 4j^2 - 1}, \quad (\text{A2})$$

$$C(i, j) = -\frac{1}{2} \ln \frac{4i^4 + 8i^2j^2 - 8ij + 4j^4 + 1}{4i^4 + 8i^2j^2 + 8ij + 4j^4 + 1}. \quad (\text{A3})$$

¹ Y. Martin and H. K. Wickramasinghe, *Appl. Phys. Lett.* **61**, 4723 (1987).

² H. J. Mamin *et al.*, *Appl. Phys. Lett.* **53**, 1563 (1988).

³ P. Grütter *et al.*, *J. Vac. Sci. Technol. A* **6**(2), 279 (1988).

⁴ D. Rugar *et al.*, *J. Appl. Phys.* **68**, 1169 (1990).

⁵ C. Schönenberger and S. F. Alvarado, *Z. Phys. B* **80**, 373 (1990).

⁶ U. Hartmann, *J. Vac. Sci. Technol. A* **8**, 411 (1990).

⁷ A. Wadas, P. Grütter, and H.-J. Güntherodt, *J. Vac. Sci. Technol. A* **8**, 416 (1990).

⁸ H. J. Mamin *et al.*, *Appl. Phys. Lett.* **55**, 318 (1989).

⁹ U. Hartmann, *Phys. Rev. B* **40**, 7421 (1989).

¹⁰ W. Williams *et al.*, *Geophys. J. Int.* **111**, 417 (1992).

¹¹ An ideal tip would bring the uncompensated magnetic "charges" as close as possible to the surface of the sample (Ref. 5).

¹² T. Göddenhenrich *et al.*, *J. Microsc.* **152**, 527 (1988);

T. Göddenhenrich (unpublished).

¹³ T. Albrecht, P. Grütter, D. Horne, and D. Rugar, *J. Appl. Phys.* **69**, 668 (1991).

¹⁴ W. F. Brown and E. A. LaBonte, *J. Appl. Phys.* **36**, 1380 (1965).

¹⁵ E. A. LaBonte, *J. Appl. Phys.* **40**, 2450 (1969).

¹⁶ A. Aharoni, *Phys. Status Solidi* **16**, 1 (1966).

¹⁷ D. Berkov, K. Ramstöck, and A. Hubert, *Phys. Status Solidi A* **137**, 207 (1993).

¹⁸ S. W. Yuan and H. N. Bertram, *IEEE Trans. Magn.* **MAG-25**, 2031 (1992).

¹⁹ W. H. Press *et al.*, *Numerical Recipes in C* (Cambridge University Press, Cambridge, 1988), Chap. 15.

²⁰ M. R. Scheinfein *et al.*, *Phys. Rev. B* **40**, 3395 (1991); M. R. Scheinfein and J. L. Blue, *J. Appl. Phys.* **69**, 7740 (1991).

²¹ A. Hubert, *Phys. Status Solidi* **32**, 519 (1969).

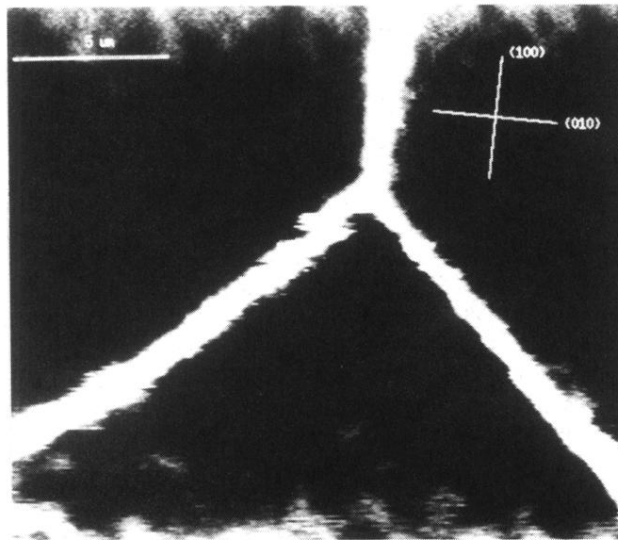


FIG. 1. MFM image of a 180° (Bloch) wall forking into two 90° walls in a 50 nm thick Fe (100) film. The film was covered by 30 nm ZnS. The scanning height was about 50 nm above the outer ZnS surface. According to our experiments, all noncharged walls give the same white contrasts.

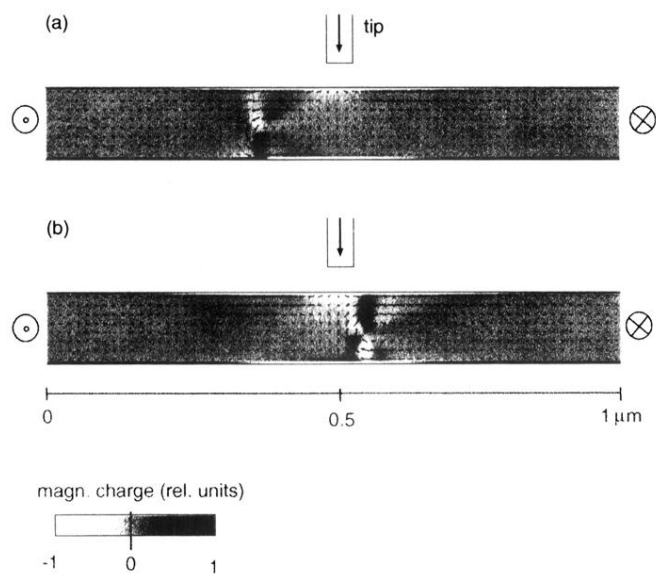


FIG. 11. A polarized counterclockwise rotating wall (b) and a polarized clockwise rotating wall (a) are both polarized by the tip stray field. The wall position differs with respect to the tip position.

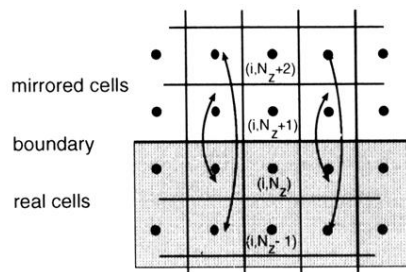


FIG. 2. The boundary condition $\partial \mathbf{m} / \partial \mathbf{n}$ can be fulfilled by a continuation with mirrored cells outside the actual boundary.

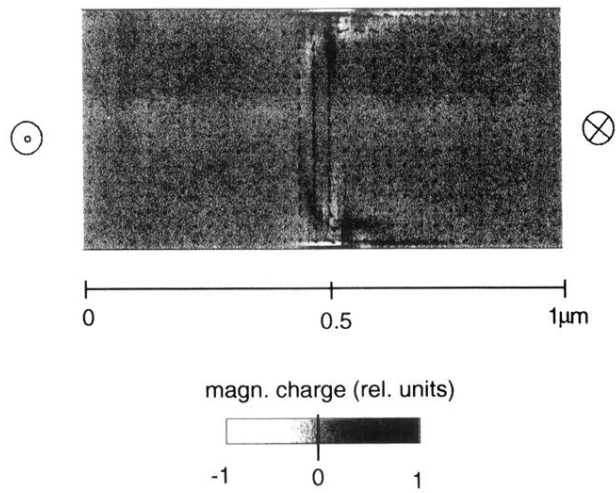


FIG. 4. Asymmetric Bloch wall in a $500 \text{ nm} \times 2000 \text{ nm}$ (100) iron slab as calculated by the model. The final grid had 256×64 cells. The picture shows only the central part ($0.5 \mu\text{m} \times 1 \mu\text{m}$) of the slab. The cells are rendered according to the magnetic charge distribution while the arrows show the projection of the magnetization \mathbf{m} into the x - z plane. In the figure only the central part of the system containing the wall is shown.

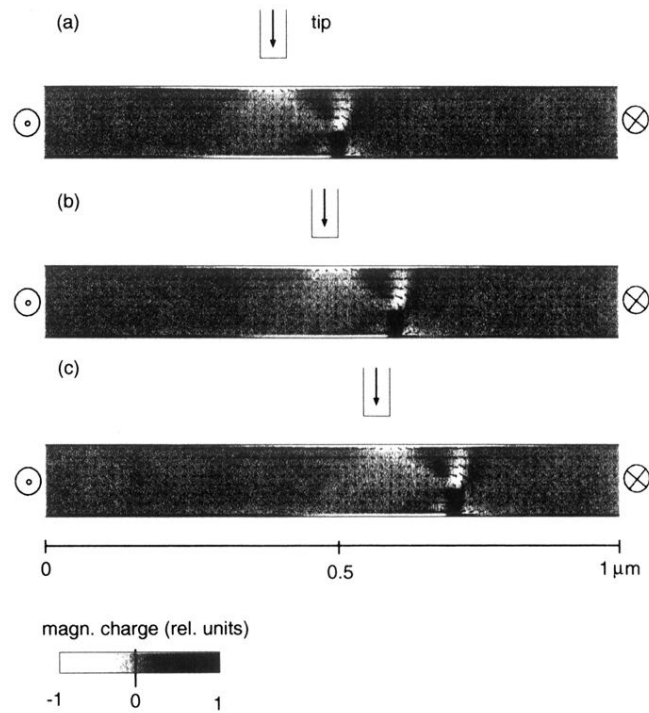


FIG. 9. Series of profiles for polarized walls. The polarization is caused by the tip stray field; the tip position above the sample is varied. The tip is simulated by a 50 nm wide Ni stripe of infinite extent in the z direction and scanning 50 nm above the sample surface. The magnetic charges compensating the charges in the image reside at both side faces and are not shown therefore, because only the central part ($1 \mu\text{m}$ of the $2 \mu\text{m}$ wide slab) of the slab is shown.